Thermal Operational Map of an ESP-In-Skid Motor: A CFD Approach

Segantine EJ[1], Romero OJ[2], Ribeiro DC[2]*, Pereira FAR[3] and Ribeiro MP[4]

[1]Master´s Program in Energy, Federal University of Espírito Santo, São Mateus, Espírito Santo, Brazil

[2]Department of Engineering and Technology, Federal University of Espírito Santo, São Mateus, Espírito Santo, Brazil

[3]Department of Industrial Technology, Federal University of Espírito Santo, Vitória, Espírito Santo, Brazil

[4]Petrobras Research Center, Rio de Janeiro, RJ, Brazil

*Corresponding author: Daniel da C Ribeiro, Department of Engineering and Technology, Federal University of Espírito Santo, São Mateus, Espírito Santo, Brazil, Tel: 2733121573; Email: daniel.ribeiro@ufes.br

Abstract

The production of oil in offshore wells has used artificial lifting methods in order to maintain or increase production. In this sense, several established methods for onshore production, such as electrical submersible pumping (ESP), have been implemented in offshore scenarios and, as a consequence, new challenges and needing improvements to optimize production in this type of environment had to be faced. Many studies concern the gas-liquid flow inside de pump but avoid include the motor and its thermal management. In this context, this study focused to assess the complex flow around an ESP motor installed in subsea skids on the seabed (Skid-ESP) through the analysis of their operational and geometric conditions using a computational fluid dynamics (CFD) tool. The main question is: is it possible to create a thermal operational map of the motor in function of motor frequency with CFD tools? The Volume-of-Fluid (VOF) model was applied together with a homogeneous heat transfer (shared temperature field among phases) coupled to the heat conduction inside motor. This approach is known as Conjugate Heat Transfer (CHT). The ESP motor is modeled as a homogeneous and isotropic body with constant volumetric heat generation. The flow analysis was performed applying the model on an industrial scale with incompressible oil and gas in in-situ conditions and considering the heat transfer between the fluid mixture and the its boundary conditions (seawater constant temperature of 4°C and variable motor heat flux as function of motor frequency). The motor frequency range considered was between 40 and 60 Hz. Since the model used was 3D, hot spots were observed at the low part of near seal motor side for gas volume fraction above 3.5%. The employed methodology was able to determine the thermal operational map with a 5% average deviation from field data.

Keywords: Electrical Submersible Pump; Field Data; Conjugate Heat Transfer; Volume-of-fluid; Gas-liquid Flow

Introduction

Oil production systems in offshore wells often require methods to maintain or increase production such as artificial lift methods, such as ESP (electrical submersible pumping) or PCP (progressive cavity pumping). In conventional ESP systems, the electric motor-centrifugal pump assembly is located inside the production column [1]. In both onshore and offshore situations, ESP is economically disadvantageous due to high intervention operation cost, since it is necessary to stop production to remove the production column [2]. According to Urban, et al. [3], the first alternative system for using ESP pumps outside the well, and therefore decoupled from the production column, is known as MOBO (subsea pumping module), where the pump is installed at the bottom of a false well in the seabed. According to Roberto, et al. [4], a new system was subsequently developed, called the ESP-in-skid represented by Figure 1. In the ESP-in-skid the pumping device is housed in the seabed a few meters ahead a subsea wellhead downstream, whose main purpose is to reduce the subsea satellite well equipment intervention costs. The main components of the ESP-in-skid are: (1) the pump module (ESP in pink inside a skid, in yellow) and (2) the flowbase (or pump support) represented in Figure 1. According to Roberto, et al. [4], the flow base component design allows an installation and recovery independent of the pumping module. The flow base has a bypass module to maintain production during a pump module intervention. This system consists of vertical connectors (VCM - Vertical Connectors Module), hydraulic actuators for opening and closing valves in the event of failure, ROV panel, production lines, umbilical connectors (UTM - Umbilical Termination Module) and installation tool. The pumping module houses two ESP capsules in an "X" configuration, with 5 ° inclination in relation to the horizontal plane and they are connected in series [4].
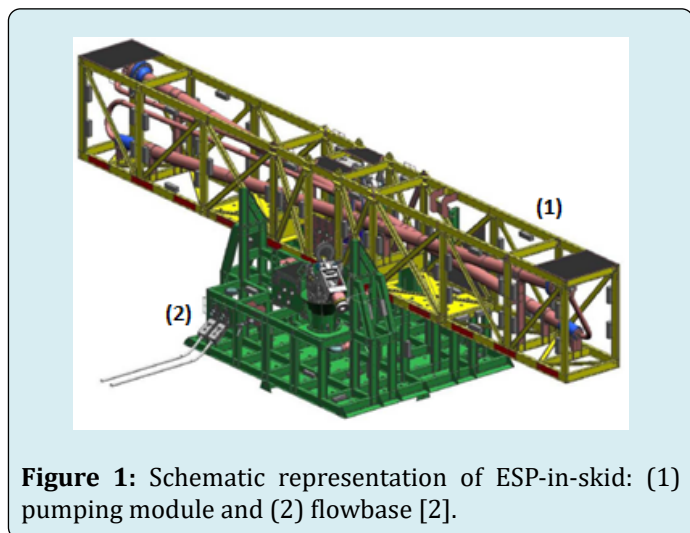

Figure 1: Schematic representation of ESP-in-skid: (1) pumping module and (2) flowbase [2].

According to the study by Tarcha, et al. [2], the main advantages offered by ESP-in-skid are: lower ESP installation costs and easier intervention operations, as the system is outside the well; the production loses are reduced due to the two pumps serial configuration with a bypass. When an intervention is necessary, one of the ESPs may continue to produce and the system operation can be maintained during ROV interventions. On the other hand, the main system disadvantage is the recommendation for pumping the production fluid with a maximum gas-fraction that is allowed to operate the ESP pump, which are 35% for the ESP-in-skid and 40% for the MOBO. The use of the ESP in subsea satellite wells with a high gas concentration causes pump problems and reduces their average time between failures (MTBF). Some identified problems are associated with the gas lock phenomenon, characterized by the passage of large gas-fractions in conventional pumps leading to non-ideal operating conditions [5]. A high gas-fraction may also overheat the ESP motor leading to a poor motor cooling, which also reduces the average time between failures (MTBF).

Most fluid flow ESP studies Ofuchi E, et al. [6] Deshmukh D, et al. [7] Peng L, et al. [8] are focused in the isothermal flow inside the centrifugal pump. Few studies are found in the literature with the aim to model the thermal ESP motor behavior.

Rodriguez, et al. [9] performed a parametric analysis using the commercial code CFX 4.2 to verify the equipment thermal behavior following the classic rule of shroud/motor configuration for heavy oils (viscosity of 78 cP @ 320 K). The authors concluded that for that oil a speed of 0.85 m/s (2.8 ft/s) should be maintained instead of 1 ft/s. In addition, the inclusion of slots in the shroud to redistribute the flow may improve the thermal motor cooling.

O'Bryan, et al. [10] validate and optimize the temperature field inside an electric motor using a CFD tool to model with a 5% experimental margin concordance. The simulation results were used to optimize the electric motor design.

Lin, et al. [11] developed a coupled flow and heat transfer model which was compiled in C code and validated by field measurements. The numerical calculation results show that marine environment factors, the heat emitted by pump and cable, and the Joule-Thomson effect have significant impact on the wellbore temperature and pressure distribution. When temperature decreases due to a low water cut condition and high gas-oil ratio, a resulted gas-fraction increase and a fluid density decrease will reduce the ESP pump pressure.

Betonico, et al. [12] studied the oil viscosity and water cut effect on the maximum motor temperature. The results

showed the motor temperature rises as the motor speed is increased. It was also shown that neglecting the effect of the thermal boundary layer development on the motor surface may result in an overheated motor prediction where actually, the motor maximum temperature is much lower than its upper limit. It was observed that fully developed temperature profile models suffer from inaccuracy when used in viscous oil applications due to their great thermal entry length.

Martins, et al. [13] employed a Computational Fluid Dynamics (CFD) code to solve the governing equations of the turbulent heat transfer single-phase flow in the ESP motor annulus space. The standard kappa-epsilon model with the Enhanced Wall Treatment (FLUENT, 2013) is used as a turbulence closure problem. This study considered flow rates range of 2200-4200 m^3/d (representing Reynolds numbers range of 27,000-133,000 approximately), Prandtl numbers 7-37, together with the wall boundary conditions of the constant temperature on the motor surface (130 °C) and capsule (quiescent seawater @ 4 °C). The authors observed that if the constant heat flux condition were used, the motor temperature would have lower values at the beginning and higher at the end of the geometry. Therefore, the higher the Nusselt number, the greater the heat transfer, which intensifies the electric motor cooling.

None of the previous works presented an analysis of the ESP motor thermal management at the seabed conditions since ESP are usually installed in the bottomhole. Therefore, this study aims to construct a thermal operational map of a ESP motor installed in the seabed through the analysis of real operational and geometric conditions using computational fluid dynamics (CFD) tools. The CFD model considers incompressible two-phase turbulent flow model (gas and liquid) with heat transfer among the fluids, the motor and seawater. Fluids (based on the oil reported by Tarcha, et al. [2] properties were based on classical empiric correlations.

Methodology

The methodology of this work consists of applying an industrial scale fluid flow model. The model includes conjugate heat transfer applied to a full-scale system and compared with field data at various operational points. The heat generation and conduction are modeled coupled to the two-phase flow advection. The motor is modeled as a homogeneous heat generation body with isotropic properties.

In the following sections, the governing equations for the two-phase flow and the motor heat conduction will be presented together with its respective relations and properties. Further, the geometry and mesh descriptions along with the boundary conditions will be presented.

Finally, the numerical aspects used will be discussed.

Mathematical Modelling

Two-phase flow model: The governing equations are based on the momentum, mass and energy conservation principles. Since the system is made up of two immiscible fluids, additional hypotheses are necessary to the equations. In the present work, the homogeneous flow hypothesis was considered, i. e., the fields (velocity, pressure and temperature) considered in the model are shared between the phases. The properties (density, viscosity, thermal conductivity, specific heat) are average weighted by the local volumetric fraction. In addition, the RANS (Reynolds Averaged Navier-Stokes) approach was adopted, requiring a turbulence closure model.

Equations (1) e (2) represent global mass and momentum conservation respectively in the Navier-Stokes formulation [14].

$$\frac{\partial \rho}{\partial t} + \nabla . \left(\rho \vec{v} \right) = 0 \quad (1)$$

where ρ is the two-phase mixture density and $\vec{v}$ is the two-phase mixture velocity vector.

$$\frac{\partial}{\partial t} \left(\rho \vec{v} \right) + \nabla . \left(\rho \vec{v} \vec{v} \right) = -\nabla p + \nabla . \mu \left[\nabla \vec{v} + \left(\nabla \vec{v} \right)^{\tau} \right] + \rho \vec{g} \quad (2)$$

The left-hand side terms in both equations represent the total acceleration. The right-hand side terms of equation (2) represent the pressure forces, viscous forces and gravitational forces, respectively. τ is the stress tensor. The property μ is the effective two-phase mixture viscosity. The gravity acceleration vector is (-0.8549978, -9,77267, 0) m/s^2, which is equivalent to an upward 5° axis inclination to the horizontal. Due to the presence of the second fluid, it is necessary to use another equation to describe the interface position between the two fluids. The equation used here is the mass conservation for the liquid phase. This approach is known as Volume-of-Fluid (VOF) and was introduced by Hirt e Nichols.

$$\frac{1}{\rho_l} \left[\frac{\partial}{\partial t} \left(\alpha_l \rho_l \right) + \nabla . \left(\alpha_l \rho_l \vec{v} \right) = 0 \right] \quad (3)$$

where α_l is the liquid volume fraction. Therefore, VOF method introduces two additional unknown variables to the system, α_l e α_g (gas volume fraction), subjected to the constraint:

$$\alpha_l + \alpha_g = 1 \quad (4)$$

The employed energy conservation equation (5) was simplified using the hypothesis of thermal equilibrium between the phases. This is equivalent to impose no thermal

resistance in the interface. In another words, the temperature field is shared among the fluids.

$$\frac{\partial \rho E}{\partial t} + \nabla \cdot \left(\vec{v} \cdot \left(\rho E + p \right) \right) = \nabla \cdot \left(k_{ef} \nabla T \right) \quad (5)$$

$$E = h - \frac{p}{\rho} \quad (6)$$

$$h = \int_{T_{ref}}^{T} c_p dT \quad (7)$$

Equation (6) is the definition of total energy (neglecting kinetic energy term) and Equation (7) is the enthalpy definition which connects the energy conservation and temperature. k_{ef} is the effective two-phase mixture thermal conductivity; c_p is the two-phase mixture specific heat. These properties are evaluated using mixing rules weighted by mass fraction, see item 2.3.1.

Thus, the system presents a zero degree of freedom because the number of unknown variables $\left(\vec{v}, p, \alpha_l, \alpha_g, e, T \right)$ is equal to the number of equations (1) to (5) [15].

Motor heat conduction model: To model the motor heat conduction, the hypothesis of homogeneous and isotropic material was employed. The properties (density, thermal conductivity and specific heat) as well as the component part volume were presented by Betônico [12] for each motor section, see 2.3.2. The motor energy conservation equation is:

$$\frac{\partial T}{\partial t} = \frac{k_m}{c_{p,m} \rho_m} \nabla^2 T + \frac{Q}{c_{p,m} \rho_m} \quad (8)$$

where Q is the volumetric heat source from the motor and the index m are the motor mixture properties.

Turbulence Closure Model

Turbulence model: The $k - \omega$ SST (Shear Stress Transport) model is employed in this work. This model is based on the eddy viscosity concept using two transport equations. The two equations describe: turbulent kinetic energy (k) transport, Equation (9), and turbulent kinetic energy dissipation frequency (ω), Equation (10):

$$\frac{\partial (\rho k)}{\partial t} + \nabla \cdot (\rho \vec{v} k) = \nabla \cdot \left[\Gamma_k \nabla_k \right] + G_k - Y_k \quad (9)$$

$$\frac{\partial}{\partial t} (\rho \omega) + \nabla \cdot (\rho \vec{v} \omega) = \nabla \cdot \left[\Gamma_\omega \nabla \cdot \omega \right] + G_\omega - Y_\omega + D_\omega \quad (10)$$

where G_k e G_ω are the generation terms for the turbulent kinetic energy and the turbulence kinetic energy dissipation frequency, Y_k e Y_ω are the dissipation terms of k e ω, e D_ω is the cross-diffusion term. All these terms are defined in Menter [16]. All properties are taken as mixture described in item 4.3.1. The diffusivities Γ_k e Γ_ω are defined in the same way, with respective Prandtl numbers σ_k e σ_ω using the following relation:

$$\Gamma_i = \mu_m + \frac{\mu_t}{\sigma_i} \quad (11)$$

where μ_t is the turbulent viscosity and μ_m is the two-phase mixture viscosity as described in item 4.3.1. The eddy viscosity is based on the Bradshaw hypothesis [17] which states that for a boundary layer flow the Reynolds stresses are proportional to the turbulent kinetic energy, as shown in equation (12).

$$\mu_t = \frac{\rho \kappa}{\omega} \frac{1}{\max \left(1 / a^* ; SF_2 / a_1 \omega \right)} \quad (12)$$

Where a^* a_1, e F_2 are defined in Fluent [18]. S is the mean flow strain rate.

The effective viscosity is defined by:

$$\mu = \mu_m + \mu_t \quad (13)$$

The effective viscosity is used in Equation (2).

Turbulent heat convection: When the convective heat transfer is in turbulent regime, the effective thermal conductivity is given by:

$$k_{ef} = k + \frac{c_p \mu_t}{pr_t} \quad (14)$$

where c_p is the two-phase mixture specific heat, k is the two-phase mixture thermal conductivity and Pr_t is the turbulent Prandtl number with constant value of 0.85.

Physical Properties

Fluids properties: The mixing rules are dependent of phases volume fractions. For mixture density ρ and mixture viscosity μ_m are defined as:

$$\rho = \alpha_g \mu_g + \alpha_l \rho_l \quad (15)$$

$$\mu_m = \alpha_g \mu_g + \alpha_l \mu_l \quad (16)$$

For each property, a specific correlation was used according to oil characteristics. The Gas-Oil Ratio (GOR) of the API 20° oil described by the Tarcha, et al. [2] work, was 50 sm^3/sm^3. For most correlation used, the specific gravity (SG) is needed and this information was neglected in the Tarcha, el al. [2] work, which an arbitrary value of 0.65 was applied.

For the thermodynamic properties (bubble point, solubility ratio, formation volume factor and viscosity),

Ribeiro DC, et al. Thermal Operational Map of an ESP-In-Skid Motor: A CFD Approach. Pet Petro Chem Eng J 2022, 6(3): 000305.

Copyright© Ribeiro DC, et al.

DeGhetto, et al. [19] correlation was employed since it is recommended for oils with degree API less than 22. The calculation of the gas thermal conductivity was based on the hypothesis that the gas was constituted of pure methane. The NIST (U.S. National Institute of Standards and Technology) [20] database was used for this property. The compilation of all properties correlations is presented in Table 1.

Property		Fluid		Correlation
Density		Liquid		DeGhetto, et al. [19]
		Gas		DeGhetto, et al. [19]
Viscosity		Liquid		DeGhetto, et al. [19]
		Gas		DeGhetto, et al. [19]
Specific Heat		Liquid		Gambill [21]
		Gas		Moshfeghian [22]
Thermal Conductivity		Liquid		Cragoe [23]
		Gas		NIST [20]

Table 1: Empirical correlation for fluid properties calculation.

The fluids properties depend on motor operation point. For this analysis were chosen four operational rotation conditions which correspond to four different frequencies of the electrical motor: 40 Hz, 45 Hz, 55 Hz and 60 Hz. Table 2 shows the values for each property for each motor frequency operational condition.

Property		Fluid		40 Hz		45 Hz		55 Hz		60 Hz
Density (kg/m^3)		Liquid		900.00		894.00		875.80		869.74
		Gas		50.57		61.43		84.88		-
Viscosity (Pa.s)		Liquid		0.05985		0.05239		0.03290		0.02584
		Gas		0.0000122		0.0000126		0.0000138		-
Specific Heat (J/kg.K)		Liquid		1844		1844		1850		1850
		Gas		2593.2		2641.5		2748.1		-
Thermal Conductivity (W/m.K)		Liquid		0.12306		0.12306		0.12282		0.12260
		Gas		0.039336		0.040560		0.043910		-

Table 2: Fluid properties obtained from Table 1 correlations for each motor frequency operational condition.

The missing properties in the 60 Hz column are due to the fact that at this condition the oil is undersaturated or all gas is in solution.

Motor physical properties: The motor physical properties were taken from Betonico [12] work. The author describes all internal parts of the motor and their properties. In order to assume a homogeneous and isotropic material, a volume weighted mean of each motor component was adopted. The volume weighted mean properties are listed in the Table 3 below.

Property	Value
Density [kg/m^3]	4623.4
Specific Heat [J/(kg K)]	996.2
Thermal Conductivity [W/(m K)]	25.1

Table 3: Motor volume-weighted mean properties.

Geometry, Mesh and Boundary Conditions

The system geometry and boundary conditions were collected from literature (Tarcha, et al.) [2] and field data.

Ribeiro DC, et al. Thermal Operational Map of an ESP-In-Skid Motor: A CFD Approach. Pet Petro Chem Eng J 2022, 6(3): 000305.

Copyright© Ribeiro DC, et al.

The motor geometry, motor OD, motor length, motor position inside capsule, seal side and position and other relevant parts of the ESP-in-skid were provided by Petrobras SA and Schlumberger's ESP catalogue for pumping unit series 738 with 750 hp [24]. The final schematic of the ESP is presented in the Figure 2.
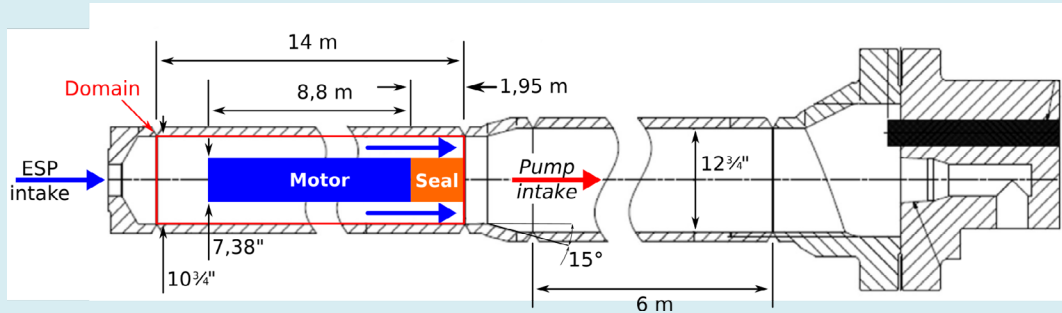

Figure 2: Schematic of the ESP-in-skid capsule and main dimensions. Fluid domain, motor and seal are highlighted. Adapted from Tarcha, et al. [2] and Schlumberger [24].

The red rectangle depicts the external limits (boundaries) of the fluid domain (volume where the mathematical model was solved). The blue arrow (ESP intake) indicates the gas-liquid mixture inlet boundary and is positioned on the left side of the fluid domain. The red arrow (Pump intake) denotes the fluids outlet boundary located at the fluid domain right side. In the real equipment, this boundary is just before the pump intake. The upper and bottom boundaries are solid walls which models the capsule external casing which is in contact with seawater. The internal boundaries are the motor and seal surfaces.

The blue rectangle (Motor) represents the solid domain. In this domain will be applied the heat conduction model with heat generation. The orange rectangle (Seal) is an adiabatic region and represents the motor seal (motor-pump separator).

The capsule is tilted 5° w.r.t. horizontal plane.

The computational mesh was built with solely hexahedra elements. To simplify the model, the motor and the seal were considered perfect cylinders. This simplification allowed to use a reduced number of elements (390,160) for applying to this geometry 12 radial equally spaced elements in the annular region as shown in Figure 3. The minimal orthogonal quality is 0.7022 and the maximum aspect ratio is 9.67.
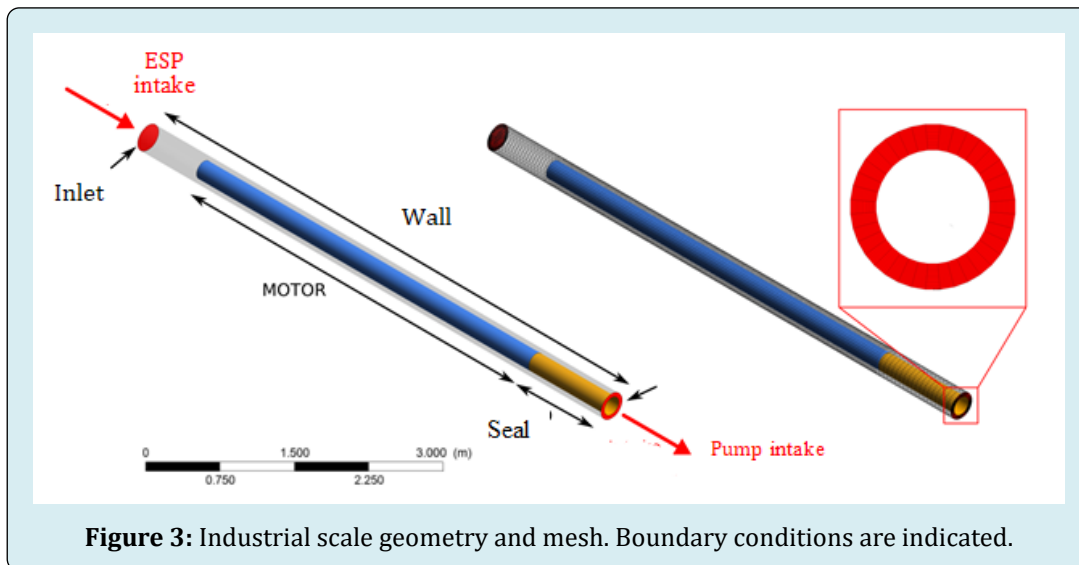

Figure 3: Industrial scale geometry and mesh. Boundary conditions are indicated.

The operational points for each case considered for this simulation is summarized in Table 4. The operational point 60 Hz is a single-phase flow because all gas is dissolved in the oil at the ESP intake due to a fluid pressure considered to be above the bubble point, 98 bar, from DeGhetto, et al. [19] correlation. As the motor frequency decreases, the gas

Ribeiro DC, et al. Thermal Operational Map of an ESP-In-Skid Motor: A CFD Approach. Pet Petro Chem Eng J 2022, 6(3): 000305.

Copyright© Ribeiro DC, et al.

volume fraction increases. The 40-60 Hz range of frequencies allowed an extended gas volume fraction effect analysis on the heat transfer.

Frequency, Hz	Temperature, °C	Pressure, bar	Gas VF, %
60	33.4	103.3	0.0
55	30.4	93.6	3.5
45	27.0	68.9	17.8
40	26.8	58.2	26.3

Table 4: Industrial scale operational points.

The momentum, energy and mass boundary conditions are set based on field data and the heat generated by the motor estimated from Betonico, et al. [25]. A homogeneous mixed oil and gas fluid is considered at the ESP intake. The electrical power converted into heat was not reported for the ESP model in the Betonico, et al. [25] work. For that, the Burt, et al. [26] work was used. The authors suggest that 2% of total electrical power input is converted into heat power. This energy amount was considered to be generated equally in each volume cell inside the motor. The obtained data for each boundary condition and heat source are shown in Table 5.

Boundary		Variable		Cases			
				40 Hz	**45 Hz**	**55 Hz**	**60 Hz**
Inlet		Oil mass flow (kg/s)		26.5174	30.3841	34.1917	40.0000
		Oil flow rate (m^3/h)		100.0	114.0	127.0	150.0
		Gas mass flow (kg/s)		0.53168	0.45187	0.1207	0.0000
		Hydraulic Diameter (m)		0.2734	0.2734	0.2734	0.2734
		Turbulence Intensity (%)		5	5	5	5
		Temperature (°C)		26.8	27	30,4	33.4
		Gas Volume Fraction (%)		26.3	17.8	3.5	0
Outlet		Static Pressure (kPa)		5820	6890	9360	10330
		Hydraulic Diameter (m)		0.0856	0.0856	0.0856	0.0856
		Turbulence Intensity (%)		1	1	1	1
		Temperature (°C)		26.8	27	30.4	38.7
Motor-volume		Heat Source (W/m^3)		17310	23280	35800	52140
Seal		Heat Flux (W/m^2)		0	0	0	0
External wall		Temperature (°C)		4	4	4	4

Table 5: Industrial scale boundary conditions and heat source.

The oil mass flow is also expressed in oil flow rate (m^3/h) because this is the variable (and units) used in field operation. Furthermore, the results of temperature are also presented in function of oil flow rate.

Numerical Approach

A High-Performance Computer (HPC) with 5 nodes (2 quad-core Intel Xeon each) and 32 Gb RAM were used in transient condition simulations.

The SIMPLE (Semi-Implicit Method for Pressure-Linked) pressure-velocity coupling was used. PRESTO! and Second Order Upwind schemes were employed for the pressure and velocity interpolation respectively. To evaluate the variables gradients the Least Squares Cell Based method was applied to each cell. The Second Order Upwind was chosen to obtain the turbulent kinetic energy and the dissipation rate. The Geo-Reconstruct scheme was used to evaluate the volume fraction equation.

For all simulations, the CFL condition was attained. The Courant number is defined by the Equation (17).

$$Co = \frac{|\text{v}|\Delta t}{\Delta x} \quad (17)$$

For all cases, two modeling challenges were faced:
- Velocity profiles and flow pattern at the ESP intake domain were unknown;
- Only one pressure point measure was available from the field data, i.e., no pressure drop was available to be compared to the simulation results.

An important numerical strategy issue for this case is the fact that the fluid flow and heat conduction problems have distinct time scales. To overcome that, the following procedure to achieve a global solution was adopted:
- All fluid flow equations with timestep limited by the fluid flow problem (0,01 s for $Co = 1$) was solved until the fluid mean temperature variation at the pump intake stabilized within 1% (~130 s);
- Then, the fluid flow equations calculations were halted and a larger timestep (10 s, limited by the heat conduction problem) was used until the maximum motor temperature reaches a constant value within 1% margin (~13 h);
- Finally, the fluid flow equations calculations were re-started with the original timestep ($Co = 1$) until the fluid mean temperature at the at the pump intake stabilized within 1% margin.
- In all cases, the initial condition started from a stabilized fluid condition at 4 °C in all domains (fluid and motor).

Monitoring points were selected to control the simulations and to judge if the solution achieved or not a steady state. The selected monitoring points used were:
- Fluid mean temperature at the pump intake;
- Mean temperature at the motor surface;
- Maximum temperature inside the motor;
- Mean gas volume fraction at the pump intake;
- Gas volume inside fluid domain.

The temperatures calculated from the simulations are then normalized using the Equation (18).

$$\theta_f = \frac{T}{T_{inlet}} \quad (18)$$

The motor heating dynamics is evaluated using the resulted nondimensional temperature by the Equation (19).

$$\theta_m = \frac{T - T_{sea}}{T_{max,m} - T_{sea}} \quad (19)$$

Where $T_{max,m} = max(T)\,@\,motor\,domain$, $T_{sea} = 4°C$.
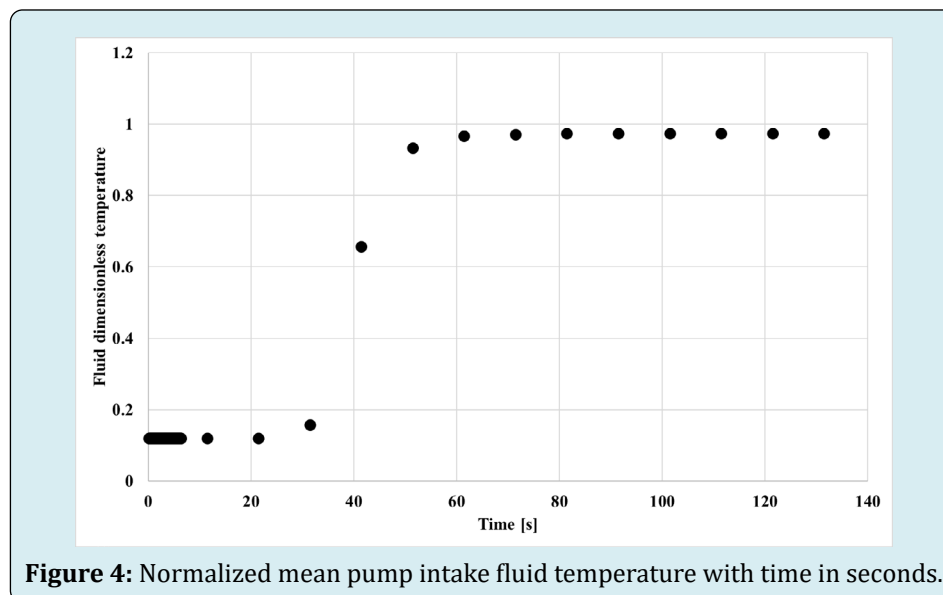
The mean temperature at motor surface is defined by:

$$T_{mean,ms} = \frac{1}{A_{ms}} \sum_{i=Cells} T_i.dA_i \quad (20)$$

Where A_{ms} is the motor surface area, the index i represents the superficial cells of motor external surface, T_i is the surface temperature and dA_i is the superficial cell area.

Results and Discussion

Motor and Fluids Heating Dynamics

The results presented in this section are the outcome of the first step of the simulation strategy for the 55 Hz case. Similar results are observed for all other cases. The fluid temperature is initially at 4 °C As can be seen in Figure 4, the fluid temperature at the pump intake reaches a constant value $(\theta_f \approx 1)$ in 60s (1 minute), whose time delay is due only to the fluid residence time inside the fluid domain volume. During this time, a little increase in the heat transfer occurs between the hot motor and the cold fluid.

Figure 4: Normalized mean pump intake fluid temperature with time in seconds.

Ribeiro DC, et al. Thermal Operational Map of an ESP-In-Skid Motor: A CFD Approach. Pet Petro Chem Eng J 2022, 6(3): 000305.

After the fluid reaches a constant temperature, the fluid flow equations solving is halted to accelerate the heat conduction in the motor. The motor heating dynamics (Figure 5) is much longer, taking, for the present case, approximately 6 h to reach 95% of the equilibrium temperature. For this reason, the time unit used in this plot is hours.
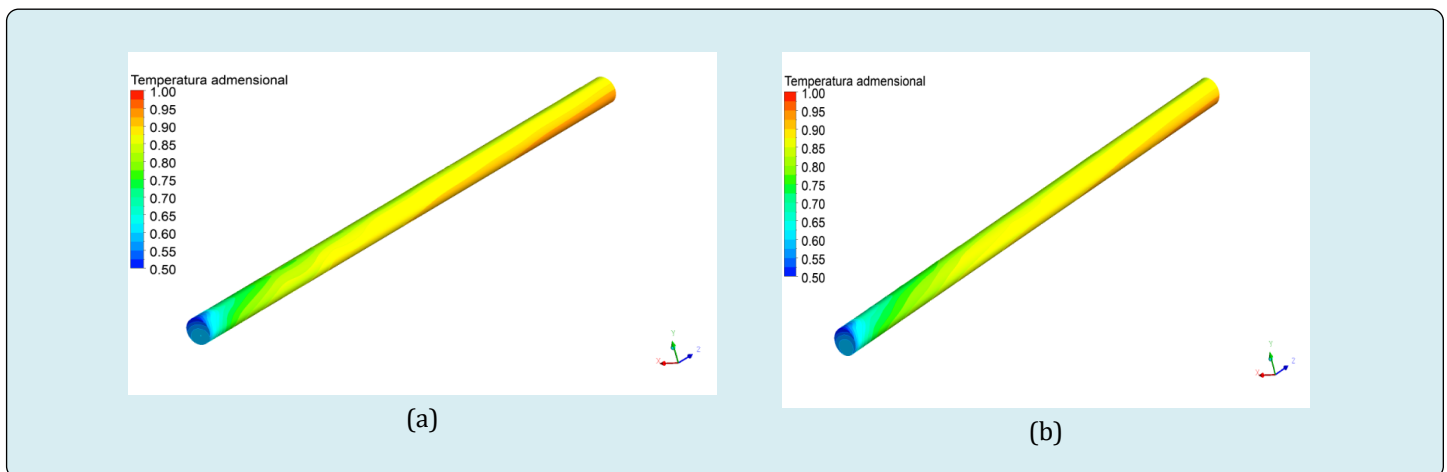

Figure 5: Dimensionless mean motor temperature at 60 Hz with time in hours.
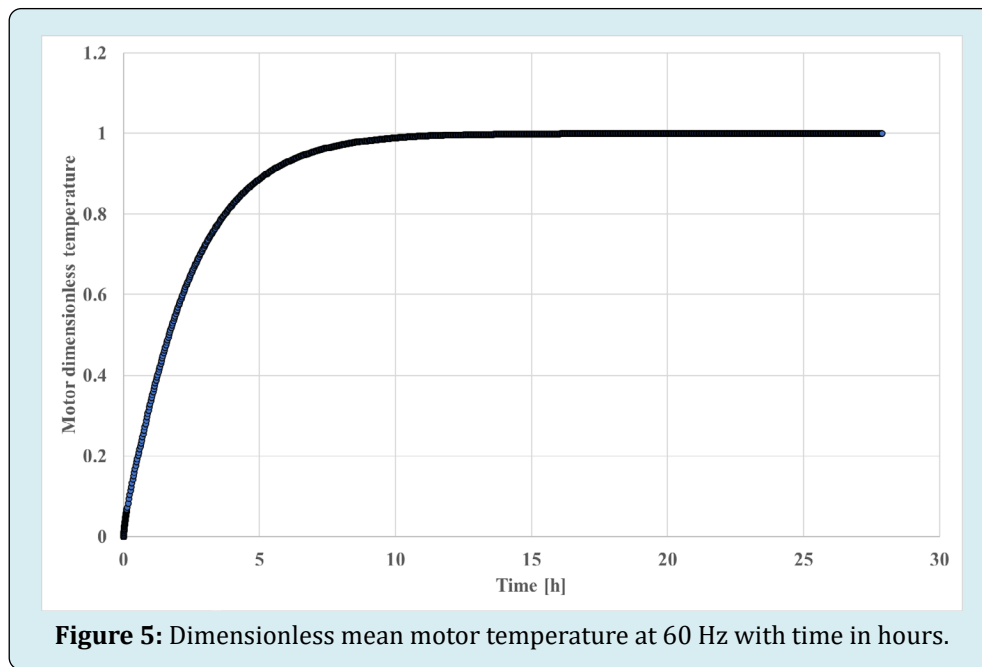
At this point, both the mean motor temperature and the pump intake fluid temperature are stabled but not at the same time. Thus, the next and last step is solving simultaneously both the fluid flow and heat conduction models.

Surface Motor Temperature Field

The motor surface temperature fields are shown in the Figure 6 where the fluid is flowing from left to right and the gravity is pointing down. The field values were evaluated using the Equation (19).

It is possible to notice that the separation of fluids causes a temperature field asymmetry in the two-phase flow cases (Figures 6 (a), (b) and (c)). When only one phase flows, the temperature field is symmetrical (Figures 6 (d)). There is also a temperature increase at the lower region of the motor top near the seal (far right of each graph in Figures 6). It also can be inferred that the turbulent flow instabilities increase the convection at the upper part of the motor bottom (far left of each plot in (Figures 6). This statement is corroborated by observing both the temperature fields and the velocity field plotted together in the Figure 7.
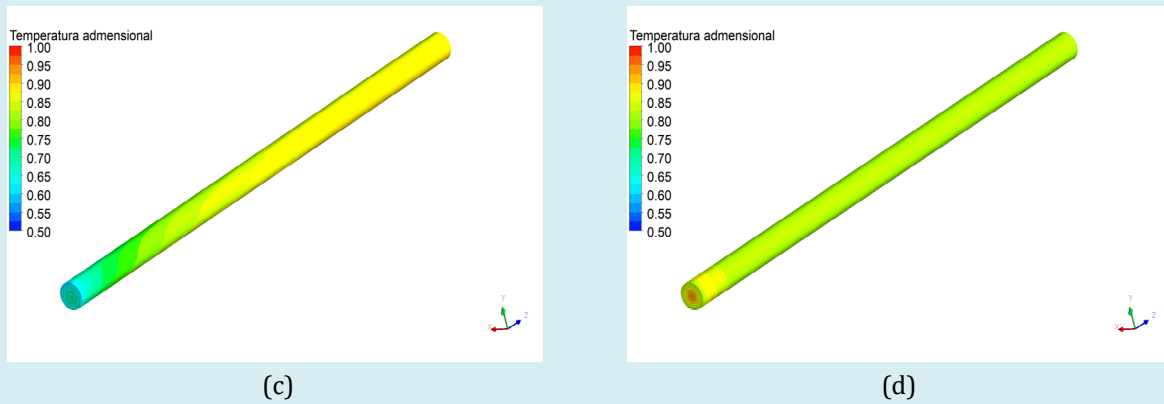

(a)

(b)

Ribeiro DC, et al. Thermal Operational Map of an ESP-In-Skid Motor: A CFD Approach. Pet Petro Chem Eng J 2022, 6(3): 000305.

Copyright© Ribeiro DC, et al.

Figure 6: Dimensionless temperature fields on the motor surface at (a) 40 Hz; (b) 45 Hz; (c) 55 Hz; (d) 60 Hz.
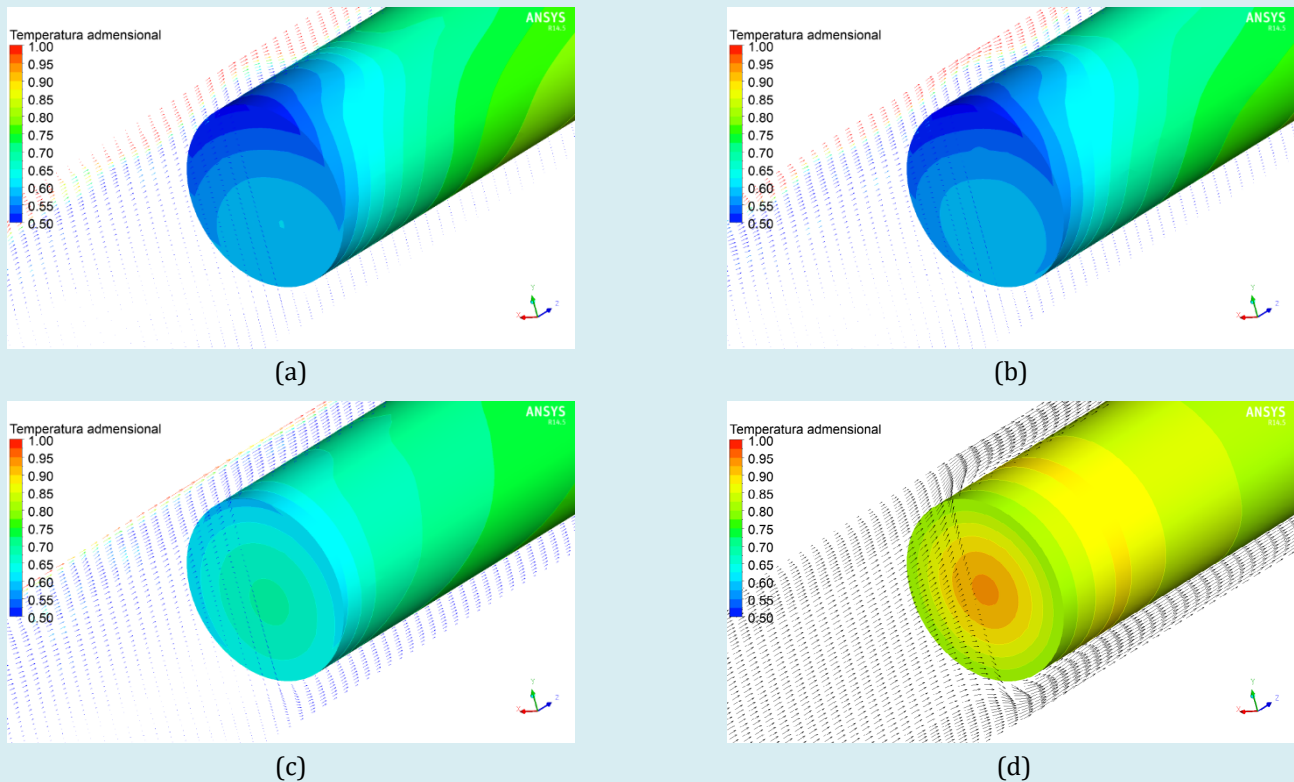

Figure 7: Dimensionless temperature fields on the motor surface and velocity vectors colored by gas volume fraction in a vertical plane: zoom at the motor bottom (inlet). (a) 40 Hz; (b) 45 Hz; (c) 55 Hz; (d) 60 Hz.

Figure 7 shows the greater the amount of gas, the greater the superficial velocities of the liquid and, consequently, the greater the convection in the upper region of the motor bottom. The single-phase case (d) shows a symmetric field as expected. Figure 8 shows the same fields as shown in the Figure 7, but at the motor top close to the seal.

As observed, the two-phase flow cases (Figure 8 (a), (b) and (c)) present an asymmetric pattern in the vertical direction. As the gas drags the liquid in the upper region, the velocities are greater which makes the convection there to be greater than in the lower region. In the lower speed case (Figure 8 (a) and (b)), a greater difference between the maximum and minimum temperature may be expected.
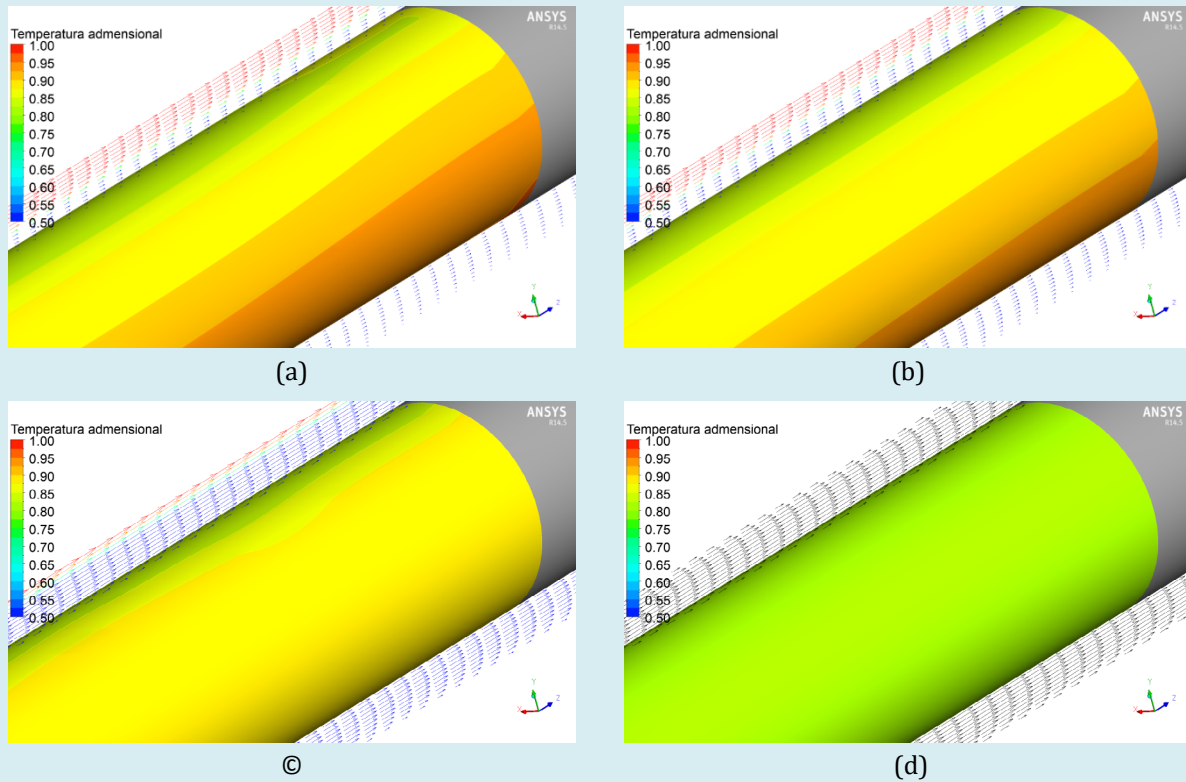
Figure 8: Dimensionless temperature fields on the motor surface and velocity vectors colored associated to the gas volume fraction in vertical plane: motor top (seal). (a) 40 Hz; (b) 45 Hz; (c) 55 Hz; (d) 60 Hz.

Velocity Field Effect on the Motor Surface Temperature

If a velocity profile along a vertical line such as that is observed in the Figure 9 for the 55 Hz case, a quantitative analysis can be made. The velocity behavior is represented by the four lines positioned along the normalized length of the motor (dimensionless ratios of 0.06, 0.30, 0.76 and 0.88). The velocity represented in the Figure 9 plots are normalized by $\left|\vec{V}\right|/\overline{V}$.
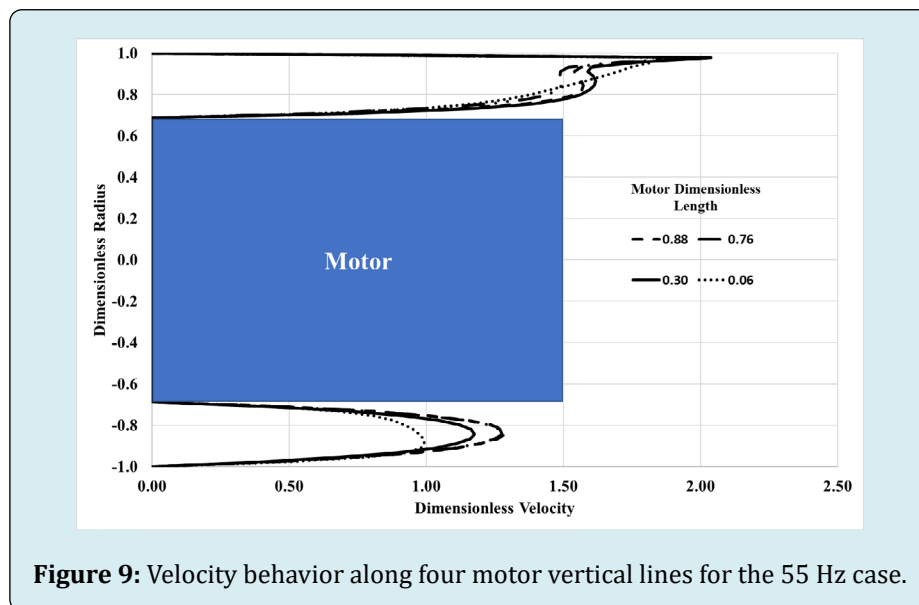

Figure 9: Velocity behavior along four motor vertical lines for the 55 Hz case.

Ribeiro DC, et al. Thermal Operational Map of an ESP-In-Skid Motor: A CFD Approach. Pet Petro Chem Eng J 2022, 6(3): 000305.

Copyright© Ribeiro DC, et al.

The speed difference between the upper and lower regions is noticeable. As convection is not only related to the speed, if there is solely gas in the upper region, the convection may not be efficient as expected. Figure 10 shows the volume fraction behavior of the gas volume fraction along the same lines of the Figure 9 for this case.

Figure 10: Gas volume fraction behavior along four motor vertical lines for the 55 Hz case.
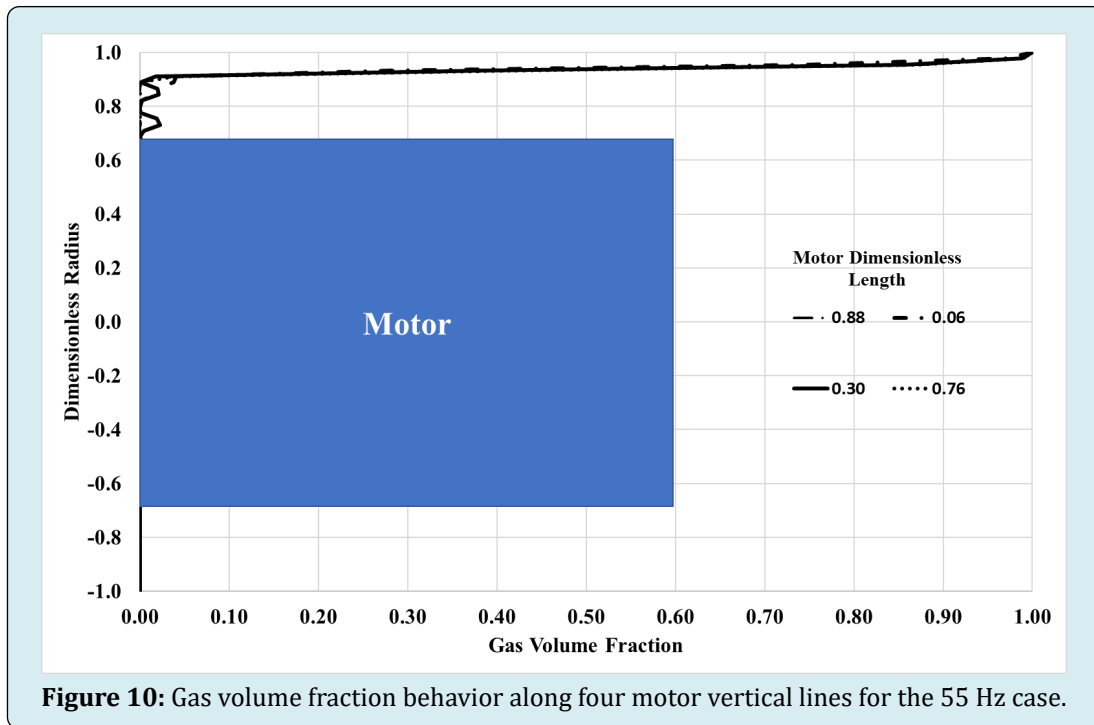
As may be observed, the gas accumulates near the outer motor wall. Therefore, the fluid contact with the motor surface is mainly composed by its liquid phase. For the purpose of a physical analysis, the gas behaves as a shroud liquid accelerator by limiting its available flow area.

Another analysis can be made involving the correlation between the temperature field inside the motor and the fluid around it for the 55 Hz case. This analysis is shown in Figure 11.

Figure 11: Motor and fluids temperature behavior along three motor vertical lines.
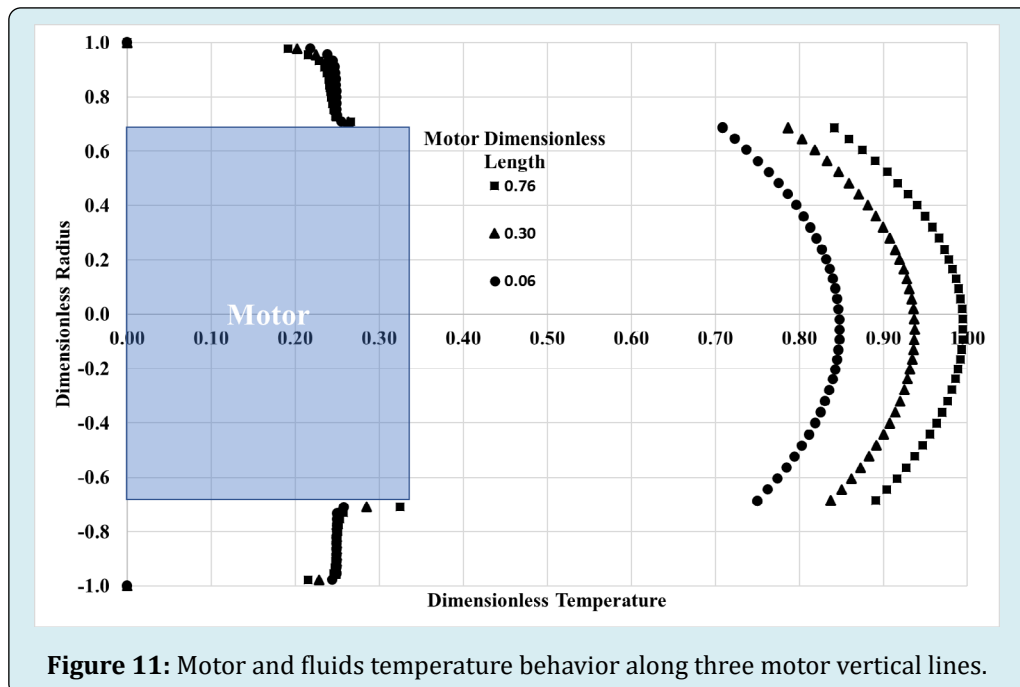
In Figure 11 temperature is normalized by the Equation (19). The fluid temperature asymmetry behavior is less clearly observed because the dimensioning scale is much higher (maximum temperature inside the motor). The fluid temperature behavior is characterized by a close sinusoidal shape, related to the characteristic of the double thermal boundary layer formed at the inner wall (motor surface) and outer wall (capsule surface). The maximum temperature calculated for the motor solid domain is close to the seal temperature (at 0.76) due to the seal adiabatic boundary condition.

Finally, Figure 12 shows the results of three characteristic system temperature analysis, including the maximum motor domain temperature.
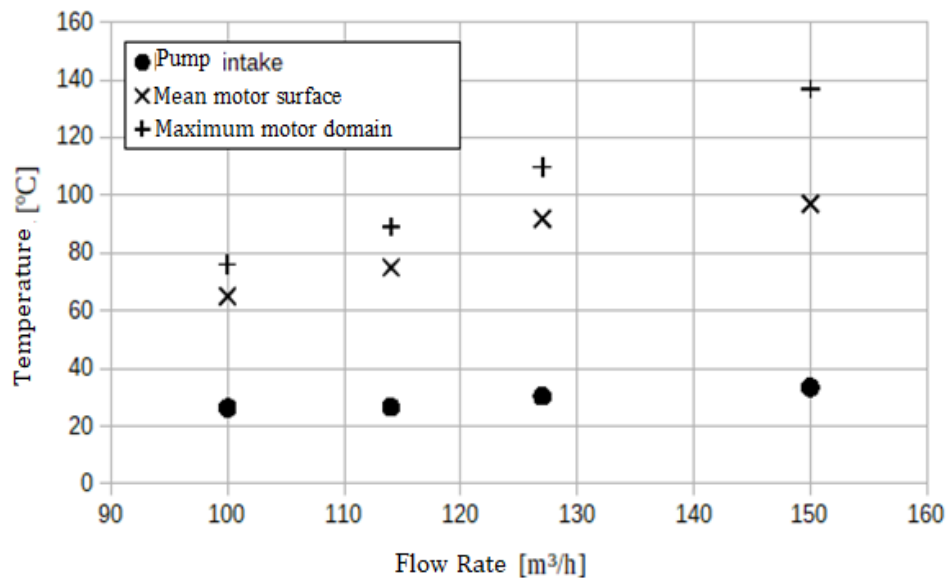

Figure 12: Fluid temperature at pump intake (fluid domain outlet), mean motor surface temperature and the maximum motor solid domain temperature in function of the production flow rate.

The higher the flow rate (or, in the present case, the frequency) the greater the heat generated and the maximum motor temperature is greater. On the other hand, the higher the flow rate, the greater the convection, since the difference between the maximum motor domain temperature (Equation (19)) and the mean motor surface temperature increases (Equation (20)). The increase in fluid temperature is not noticeable within the scale used, but it becomes more distinguished as the flow rate increases.

Simulated and Field Measured Thermal Operational Map Comparison

An estimate of the motor temperature as a function of the flow rate or the operational frequency (40 Hz, 45 Hz, 55 Hz, 60 Hz) provided by VSD (Variable Speed Drive) can be made. Figure 13 shows the numerical results, which are coherent with the field data. The results are satisfactory in spite of the uncertainties related to a mean deviation of 5% and to a maximum deviation of 10% in the 60 Hz operational case.

The difference increase between the simulated and field data as the flow rate increases, may be due to the less accurate PVT correlation properties of the related pressure and temperature operational conditions. Also, the arbitrated value for the specific gravity of the gas may be higher than the real ones. The single-phase flow assumption at the highest frequency may provide another explanation for the greater difference, since there may have additional gas in the real operational condition.
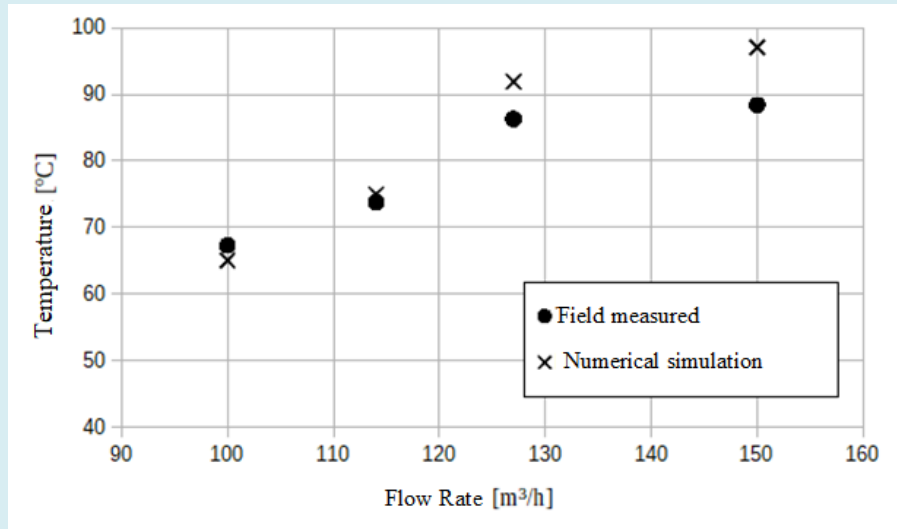
Ribeiro DC, et al. Thermal Operational Map of an ESP-In-Skid Motor: A CFD Approach. Pet Petro Chem Eng J 2022, 6(3): 000305.

Copyright© Ribeiro DC, et al.

Figure 13: Thermal operational map (Mean motor surface temperature): the numerical simulation results and field measured motor surface.

Conclusions

The proposed work was to numerically model the turbulent gas-liquid flow with heat exchange around the electric motor of a subsea Skid-ESP system, the adopted methodology was based on the use of CFD tools implemented through the ANSYS Fluent v.15.0 software, and included the employment of specific correlations to describe the oil properties associated with the real oilfield operational data.

The following conclusions may be achieved:
- In spite of the uncertainties related to a mean deviation of 5% and to a maximum deviation of 10% in the 60 Hz operational case, the developed methodology was able to construct a thermal operational map of an ESP-in-skid motor;
- The developed methodology was able to generate coherent dynamic motor's heating time data around 6 h considering a simplified assumption of a motor made of a homogeneous and isotropic material;
- Instabilities induced by the gas-liquid interface may generate low temperature data at the motor bottom, in the analyzed quasi-horizontal configuration;
- Flow stratification generates high temperatures data at the motor bottom in the region close to the seal;
- The presence of gas, in the quantities provided by DeGhetto (1995), does not favor convection.

Acknowledgement

Nomenclature

A_{ms}	Motor surface area, m^2
Co	Courant number
c_p	Two-phase mixture specific heat, J/kg/K
$c_{p,m}$	Motor specific heat, J/kg/K
D_ω	ω-equation cross diffusion term,
dA_i	Surface cell area, m^2
E	Two-phase mixture specific energy, J/kg
G_i	Turbulence model equations ($i = k$ or ω) generation terms, m^2/s^3
$\vec{g}$	Gravity acceleration vector, m/s^2
h	Two-phase mixture specific enthalpy, J/kg
k	Two-phase mixture thermal conductivity, W/m/K
k_{ef}	Turbulent two-phase mixture thermal conductivity, W/m/K
k_m	Motor thermal conductivity, W/m/K
p	Pressure, bar
Pr_t	Turbulent thermal Prandtl number
$\dot{Q}$	Volumetric heat source from the motor, W/m^3
T	Two-phase mixture Temperature, °C
T_{ref}	Reference temperature, °C

T_{inlet}	Two-phase mixture temperature at inlet, °C
T_{sea}	Sea temperature, ºC
$T_{max,m}$	Motor maximum temperature, °C
$T_{mean,ms}$	Motor surface mean temperature, °C
t	Time, s
$\vec{v}$	Two-phase mixture velocity vector, m/s
$|v|$	Velocity magnitude, m/s
Y_i	Turbulence model equations ($i = k$ or ω) dissipation terms, m²/s³
α_g	Gas volume fraction
α_l	Liquid volume fraction
ρ	Two-phase mixture density, kg/m³
ρ_g	Gas density, kg/m³
ρ_l	Liquid density, kg/m³
ρ_m	Motor density, kg/m³
μ	Effective viscosity, Pa s
μ_m	Two-phase mixture viscosity, Pa s
μ_g	Gas viscosity, Pa s
μ_l	Liquid viscosity, Pa s
μ_t	Turbulent viscosity, Pa s
k	Turbulent kinetic energy, m²/s²
Γ_i	Turbulence model equations ($i = k$ or ω) diffusivities, m²/s
ω	Turbulent kinetic energy dissipation frequency, 1/s
σ_i	Turbulent Prandtl number ($i = k$ or ω)
Δx	Equivalent control volume size, m
Δt	Timestep, s
θ_f	Dimensionless two-phase mixture temperature,
θ_m	Dimensionless motor temperature,

References

1. Viana AM, Manzela AA (2015) Avanços e Desafios em Sistemas de Bombeio Centrífugo Submerso. Revista de Engenharias da Faculdade Salesiana 2: 26-32.

2. Tarcha BA, Borges OC, Furtado RG (2015) ESP Installed in a Subsea Skid at Jubarte Field. SPE Artificial Lift Conference, Latin America and Caribbean.

3. Urban A, Boechat N, Haaheim S, Sleight N, Debacker I, et al. (2015) MOBO ESP Interventions. OTC Brasil, Rio de Janeiro, Brazil.

4. Roberto MAR, Oliveira PS, Pyramo BM (2013) Mudline ESP: Electrical Submersible Pump Installed in a Subsea Skid. Offshore Technology Conference.

5. Takacs G (2009) Electrical submersible pumps manual: design, operations, and maintenance.

6. Ofuchi EM, Stel H, Vieira TS, Ponce FJ, Chiva S, et al. (2017) Study of the effect of viscosity on the head and flow rate degradation in different multistage electric submersible pumps using dimensional analysis. J Pet Sci Eng 156: 442-450.

7. Deshmukh D, Samad A (2019) CFD-based analysis for finding critical wall roughness on centrifugal pump at design and off-design conditions. J Braz Soc Mech Sci Eng 41: 58.

8. Peng L, Wang Y, Yan F, Nie C, Ouyang X, et al. (2020) Effects of Fluid Viscosity and Two-Phase Flow on Performance of ESP. Energies 13(20): 5486.

9. Rodrigues JD, Finaish F, Dunn-Norman S (2000) Parametric study of motor/shroud heat transfer performance in an electrical submersible pump (ESP). J Energy Resour Technol Sep 122(3): 136-141.

10. O'Bryan R, Rutter R, Sheth K (2012) Validation and Optimization of Heat Transfer in The Electrical Submersible Pump Motor By CFD. ASME International Mechanical Engineering Congress and Exposition 6: 955-961.

11. Lin RY, Shao CB, Li J (2013) Study on two-phase flow and heat transfer in offshore wells. J Petrol Sci Eng 111: 42-49.

12. Betônico GC (2013) Study of temperature distribution on ESP motors. Master's Thesis, Faculty of Mechanical Engineering, Unicamp.

13. Martins JR, Ribeiro DC, Pereira FAR, Ribeiro MP, Romero, et al. (2020) Heat dissipation of the Electrical

Ribeiro DC, et al. Thermal Operational Map of an ESP-In-Skid Motor: A CFD Approach. Pet Petro Chem Eng J 2022, 6(3): 000305.

Copyright© Ribeiro DC, et al.

Submersible Pump (ESP) installed in a subsea skid. Oil & Gas Sci Technol-Rev IFP Energies nouvelles 75(13).

14. Versteeg HK, Malalasekera W (2007) An Introduction to Computational Fluid Dynamics: 2nd (Edn.), The Finite Volume Method.

15. Xu JH, Li SW, Tan J, Luo GS (2008) Correlations of droplet formation in T-junction microfluidic devices: from squeezing to dripping. Microfluid Nanofluid 5: 711-717.

16. Menter FR (1994) Two-Equation Eddy-Viscosity Turbulence Models for Engineering Applications. AIAA Journal 32(8): 1598-1605.

17. Bradshaw P, Ferriss DH, Atwell NP (1967) Calculation of boundary layer development using the turbulent energy equations. J Fluid Mech 28(3): 593-616.

18. Fluent (2013) ANSYS Fluent Theory Guide v15.0.

19. De Ghetto G, Paone F, Villa M (1995) Pressure-Volume-Temperature Correlations for Heavy and Extra Heavy Oils. International Heavy Oil Symposium, Society of Petroleum Engineers, Calgary, pp: 647–662.

20. NIST (National Institute of Standards and Technology) (2018) Chemistry web book.

21. Gambill WR (1957) You Can Predict Heat Capacities. Chem Eng 64(6): 243-248.

22. Moshfeghian M (2011) Development of a New Generalized Correlation for Natural Gas Heat Capacity. 90th Annual GPA Convention, San Antonio, Texas, USA.

23. Cragoe CS (1929) Thermal Properties of Petroleum Products. NBS Miscellaneous Publication No. 97, US Bureau of Standards.

24. Schlumberger (2017) REDA Electric Submersible Pump Systems Technology Catalog, Houston.

25. Betonico GC, Bannwart AC, Ganzarolli MM (2015) Determination of the temperature distribution of ESP motors under variable conditions of flow rate and loading. J Petrol Sci Eng 129: 110-120.

26. Burt C, Piao X, Gaudi F, Busch B, Taufik NFN, et al. (2006) Electric motor efficiency under variable frequencies and loads. ITRC report R-06-004.